Anodic behaviour and X-ray photoelectron spectroscopy of ternary tin oxides

N. Sharma, K.M. Shaju, G.V. Subba Rao, B.V.R. Chowdari*

Department of Physics, National University of Singapore, Singapore 117542, Singapore

Abstract

The compounds $SrSnO_3$, $BaSnO_3$ and Ca_2SnO_4 have been synthesized by solid-state and/or sol–gel methods, characterized by X-ray diffraction (XRD), X-ray photoelectron spectroscopy (XPS) and scanning electron microscopy (SEM) and their electrochemical properties studied as cathodes versus Li metal in the range 0.005–1.0 V. $ASnO_3$ (A = Sr, Ba), adopt the perovskite structure whereas Ca_2SnO_4 has the Sr_2PbO_4 structure. The discharge capacities (mAh g^{-1}) (moles of equivalent Li) on the 20th cycle at a current rate of 30 mA g^{-1} are: $SrSnO_3$ (solid-state) (144 (1.4)), $SrSnO_3$ (sol–gel) (222 (2.1)), $BaSnO_3$ (solid-state) (190 (2.2)), $BaSnO_3$ (sol–gel) (156 (1.8)) and Ca_2SnO_4 (247 (2.4)). The $SrSnO_3$ (sol–gel) with nano-particle morphology displays better galvanostatic cycling performance than $SrSnO_3$ (solid-state). The cycling behaviour of $SrSnO_3$ and $BaSnO_3$ is inferior to that of Ca_2SnO_4 and $CaSnO_3$, which demonstrates that 'Ca' is superior as a matrix element than Sr or Ba. The inferior electrochemical performance of Ca_2SnO_4 in comparison to $CaSnO_3$ reveals that the higher Ca:Sn ratio in the former is not advantageous and the perovskite structure is preferable to that of Sr_2PbO_4 structure. The coulombic efficiencies are >98% in all cases. Cyclic voltammetry (CV) compliments the observed cycling behaviour.
© 2004 Elsevier B.V. All rights reserved.

Keywords: $ASnO_3$ (A = Sr, Ba); Ca_2SnO_4; Anode material; Electrochemical performance; Lithium-ion battery; X-ray photoelectron spectroscopy

1. Introduction

Among the most advanced of all rechargeable power sources, lithium-ion batteries with a high specific energy have the capability to meet the ever-growing energy needs for portable electronic devices. Their performance is based on the shuttling of Li-ions between the positive (cathode) and the negative (anode) electrodes. To a great extent this process relies on the stability and current rate capability of the electrode materials. Therefore, considerable research efforts have been undertaken to develop improved electrodes.

To date graphite has been used as the anode material in lithium-ion batteries. It possesses a theoretical capacity of 372 mAh g^{-1}. After the impressive results reported for amorphous composite tin oxide (ATCO) [1], which gave a

reversible capacity of 600 mAh g^{-1}, a large variety of tin-containing compounds have been proposed as possible anode materials [2–15]. On the basis of in situ X-ray diffraction (XRD), Scanning electron microscopy (SEM) and transmission electron microscopy, it was established that the ability of Sn to form alloy with Li ($Li_{4.4}Sn$) is responsible for the electrochemical cycling. Unfortunately, however, extensive volume changes that occur during the alloying–de-alloying process cause mechanical instabilities in the electrode and result in a rapid decay in capacity after a few cycles [4]. In order to circumvent this problem, and achieve maximum reversible capacity over large number of cycles, the chemistry of the electro-active host material and its morphology have to be specifically designed. The first approach involves incorporation of the active material (Sn) in a suitable, crystalline or amorphous matrix that contains 'spectator' atoms. This can ameliorate the volume changes taking place during electrochemical cycling while taking care of inter-particle electronic

---

conductivity. The spectator atoms do not participate in the cycling process. A number of tin oxide based composites and glasses [4–7,10–18] and crystalline compounds [3,8,9,19,20] have been found to exhibit improved cycling performance in comparison with pure tin oxides (SnO or SnO_2). The importance of the spectator atom and crystal structure of the starting Sn-containing oxide has been clearly demonstrated [2,8,9].

The second approach is the manipulation of compound morphology. More specifically, nano-particles or nano-structured, thin-film Sn-based compounds have shown a combination of rate capability, cycle life and capacity superior to that of electrodes with larger particles (>5 μm size). The nano-particles appear to suffer minimal volume variations and maintain a rather stable microstructure during electrochemical cycling. Furthermore, the surface area of the nano-particle electrode will be large and therefore will cause small diffusion lengths for Li-ions and improve the rate capability [21–24].

Apart from electrode design aspects, the electrochemical performance of Sn-oxides is sensitive towards the choice of the voltage range for cycling [16,17,19,20,24]. Courtney and Dahn [17] have shown that the optimum voltage range for SnO_2-based electrodes is 0.01–0.8 V versus Li. Therefore, considering the aforementioned strategies, we have synthesized the compounds $SrSnO_3$ and $BaSnO_3$ that possess the perovskite crystal structure and have evaluated their electrochemical performance versus Li metal for possible use in lithium-ion batteries. The results are compared with those for iso-structural $CaSnO_3$ [19,20]. The effect of crystal structure and spectator atom content is evaluated by comparing the performance of Ca_2SnO_4 (Sr_2PbO_4-type structure) with $CaSnO_3$.

2. Experimental

Powders of $SrSnO_3$ and $BaSnO_3$ were synthesized by high-temperature solid-state reaction [25] and sol–gel techniques [19,20,26]. Ca_2SnO_4 was prepared by the sol–gel process. For the solid-state reaction, stoichiometric amounts of high purity $SrCO_3$ (Merck)/$BaCO_3$ (Fischer) and SnO_2 (Merck) were mixed thoroughly in an auto grinder and calcined in air at 800 °C for 6 h. After cooling to room temperature (RT), the product was re-ground, pelletized, heated at 1150 °C for 24 h in air, and slowly cooled to room temperature. The pellets were ground to a fine powder. For the sol–gel method, 0.1 M of $SnCl_2$ (Aldrich) was dissolved in 4 M ethylene glycol (Merck) at 50 °C with stirring and then 1 M citric acid (Fischer) was added. The temperature was raised to 80 °C and 0.1 M $SrCO_3$/$BaCO_3$/0.2 M $Ca(NO_3)_2 \cdot 4H_2O$ (BDH) was added and the stirring was continued for 6 h to obtain a clear solution. The solution was then heated for 12 h at 135 °C and changed into a translucent gel. It was recovered and heat treatment at 350 °C in air for 6 h caused the formation of black flakey material. The latter was ground to a fine powder and calcined in air at 800 °C for $SrSnO_3$ and Ca_2SnO_4

and at 1200 °C for $BaSnO_3$ for 6 h, followed by cooling to room temperature. $CaZrO_3$ was synthesized by the sol–gel method as described above for $SrSnO_3$ except that instead of $SnCl_2$, 0.1 M $ZrO(NO_3)_2$ (Alfa Aesar) was used. $CaSnO_3$ was prepared by the sol–gel method [19].

The crystal structure was identified by recording X-ray diffraction patterns on a Siemens D5005 diffractometer that was equipped with Cu Kα radiation. X-ray photoelectron spectroscopy (XPS) of the compounds was performed with a VG Scientific ESCA MK II spectrometer with Mg Kα radiation. The high-resolution spectra were recorded with a constant pass energy mode (20 eV). Charge referencing was undertaken against adventitious carbon, C 1s binding energy (BE) = 284.6 eV. The raw spectra were curve-fitted by means of XPS peak fit software. Complex spectra were delineated by non-linear least-square fitting with a Gauss–Lorentz (ratio 60:40) curve into multiple peaks and the binding energies were evaluated. The BEs are accurate to ± 0.1 eV. Surface morphology was investigated by scanning electron microscopy (SEM; JEOL JSM-6700F, Field Emission Electron Microscope). The electrode fabrication process is the same as reported earlier [19,20], namely by a doctor blade technique with active material ($SrSnO_3$/$BaSnO_3$/Ca_2SnO_4; synthesized by sol–gel method), super P carbon (MMM, Ensaco350) and binder (Kynar 2801) in a weight ratio of, 65:20:15. For $SrSnO_3$/$BaSnO_3$ (synthesized by the solid-state reaction), the electrodes are comprised of the respective materials in the weight ratio 80:10:10. These ratios were found to give optimum reproducible performance. A thick slurry was made using 1-methyl 2-pyrrolidone (NMP) as solvent for the binder and coated on to a copper foil. Thick-film (20–30 μm) electrodes were dried at 80 °C in an air oven, pressed between twin rollers, and cut into circular discs (16 mm diameter) followed by drying in a vacuum oven at 70 °C for 12 h. Coin cells (size, 2016) were fabricated in an argon-filled glove box, which restricted H_2O and O_2 to <1 ppm. The cells used Li metal (Kyokuto Metal Co., Japan) foil as the counter electrode, Celgard 2502 membrane as the separator, and 1 M $LiPF_6$ in ethylene carbonate (EC) and diethyl carbonate (DEC) (1:1 by volume, Merck Selectipur LP40) as the electrolyte. The cells were aged for 24 h before testing. Cyclic voltammetry (CV) and galvanostatic charge–discharge cycling of the cells were carried out at room temperature by a computer controlled MacPile II instrument (Biologic, France) and a Bitrode multiple battery tester (model SCN, Bitrode, USA), respectively.

3. Results and discussion

3.1. Characterization by XRD, SEM and XPS

The compounds $SrSnO_3$ and Ca_2SnO_4 are white, whereas $BaSnO_3$ is a light yellow powder. While $SrSnO_3$ (sol–gel) could be prepared at 800 °C, it is found that single-phase $BaSnO_3$ forms only after heating at 1200 °C. The XRD pat-
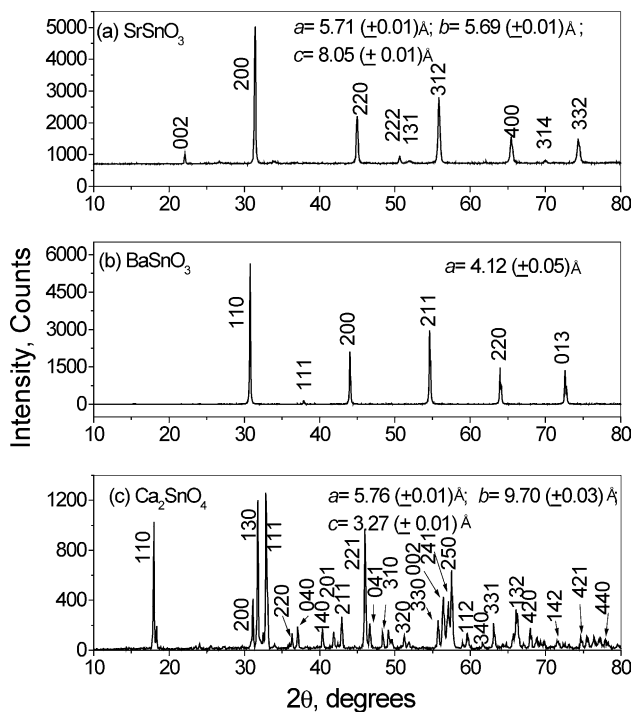
Fig. 1. Powder X-ray diffraction (XRD) patterns of SrSnO₃, BaSnO₃, and Ca₂SnO₄. Cu Kα radiation. Miller indices (*hkl*) and lattice parameters (*a, b* and *c*) are shown.

terns were recorded for all the compounds. The patterns for SrSnO₃ prepared by solid-state and sol–gel techniques are identical. This is also the case with BaSnO₃.The XRD patterns for powders of SrSnO₃, BaSnO₃ and Ca₂SnO₄ are given in Fig. 1. It is known that SrSnO₃ has an orthorhombically-distorted perovskite structure [27] whereas BaSnO₃ adopts the cubic perovskite structure [28]. This is due to the difference in the tolerance ratio for the formation of the perovskite structure even though both the compounds possess SnO₆ octahedra. The patterns were indexed and the lattice parameters were calculated by the least-square fitting method. These are also given in Fig. 1. The *a,b* and *c* parameters are in very good agreement with those reported for SrSnO₃ ([27] and JCPDS card no. 77-1798) and with the *a* value for BaSnO₃ ([26] and JCPDS card no. 74-1300). The XRD pattern of Ca₂SnO₄ is shown in Fig. 1(c) and the lattice parameters are in agreement with JCPDS card no. 74-1493. It has a crystal structure that is analogous to Sr₂PbO₄ [29,30]. The orthorhombic unit cell is comprised of infinite chains of edge-shared SnO₆ octahedra that are connected by a perpendicular network of CaO₇ monocapped trigonal prisms, the Ca-ion being in seven-fold oxygen co-ordination.

The SEM images of the compounds shown in Fig. 2 differ from each other revealing that the morphology is a function of the composition and the synthetic procedure. Electron micrographs of SrSnO₃ (solid-state) (Fig. 2(a)) show well-separated smooth particles with an average size of, 0.5–1.0 μm. A considerable size reduction is achieved by the sol–gel synthesis of SrSnO₃ (Fig. 2(b)), which yields aggre-

gates of nano-particles with size-200–300 nm. The morphology of BaSnO₃ (sol–gel) (Fig. 2(c)) shows agglomerates of sub-micron particles and this is due to the higher synthesis temperature (1200 °C) that is required for formation of the compound. The Ca₂SnO₄ is comprised of oblong particles (1–5 μm), as shown in Fig. 2(d)

It is well-known that X-ray photoelectron spectroscopy (XPS) is a powerful and non-destructive technique to ascertain the valence states of metal ions in complex compounds [31]. The core level binding energies of the metal or non-metal ions are characteristic of the oxidation state and their co-ordination in the crystal lattice. Hence, XPS has been used extensively to characterize electrode materials [32,33]. The XPS of only BaSnO₃ has been reported in the literature [34]. In this study, we have studied the XPS of ASnO₃ (A = Ca, Sr and Ba) and Ca₂SnO₄. The BEs of the various ions have been evaluated and are compared with those reported for BaSnO₃, SnO₂ and related perovskite materials. XPS core level spectra of the Sn 3d, O 1s, Ca 2p/Sr 3d/Ba 3d regions for the compounds, ASnO₃, A = Ca, Sr, Ba and Ca₂SnO₄ are given in Figs. 3–5. The BEs for all these and related compounds from the literature are listed in Table 1. The Sn 3d spectra of ASnO₃ and Ca₂SnO₄ (Fig. 3(a–d) show two peaks in the energy range, 485–495 eV and correspond to Sn $3d_{5/2}$ and $3d_{3/2}$. The peak separation, namely, $\Delta = 3d_{5/2} - 3d_{3/2} = 8.4$ eV, in all the cases indicates the correctness of the peak assignment. Manorama et al. [34] have reported only the Sn $3d_{5/2}$ peak with a BE of 486.9 eV in BaSnO₃ whereas Ayouchi et al. [35] found BEs of 487.1 eV for $3d_{5/2}$ and 495.5 eV for $3d_{3/2}$ a film that comprised both SnO and SnO₂. The XPS spectra of the core levels in the Sn 3d region of a SnO₂ film deposited on SiO₂/Si (1 0 0) showed BEs of 486.8 and 495.2 eV for Sn $3d_{5/2}$ and Sn $3d_{3/2}$, respectively [36]. It is clear from Fig. 3 and Table 1 that tin has a 4+ valency in the compounds presently studied. Since $BaSn^{4+}O_3$ has a cubic structure, it has perfect SnO₆ octahedra and the Ba^{2+} ions adopt a 12-fold oxygen co-ordination. The compounds ASnO₃ (A = Ca, Sr), Ca₂SnO₄ and SnO₂, which have distorted SnO₆ octahedra show higher BE values for both $3d_{5/2}$ and $3d_{3/2}$ as compared with BaSnO₃. This is more evident in the case of Ca₂SnO₄ and SnO₂.

The O 1s spectra for ASnO₃ (Fig. 4(a–d)) compounds show broad and asymmetric peaks and have been fitted to two overlapped peaks with BEs in the 529–531 eV region. The BEs are listed in Table 1. The overlaping peaks are indicative of two different oxygen contributions. A similar asymmetric peak in the O 1s region was observed in other perovskite oxide compounds [34,37,38]. These are generally ascribed to the lattice oxygen and adsorbed oxygen. Therefore, the peak at 528.7 eV in BaSnO₃ is attributed to the O^{2-} contribution from the perovskite anionic network. The other peak, which is lower in intensity and occurs at a higher BE, viz., 530.4 eV, is ascribed to OH^- and/or surface adsorbed oxygen. As expected, the O 1s BEs including that due to the adsorbed oxygen of ASnO₃, (A = Ca, Sr) and other perovskite oxides with A = La [37] (Table 1), which have distorted SnO₆ oxy-
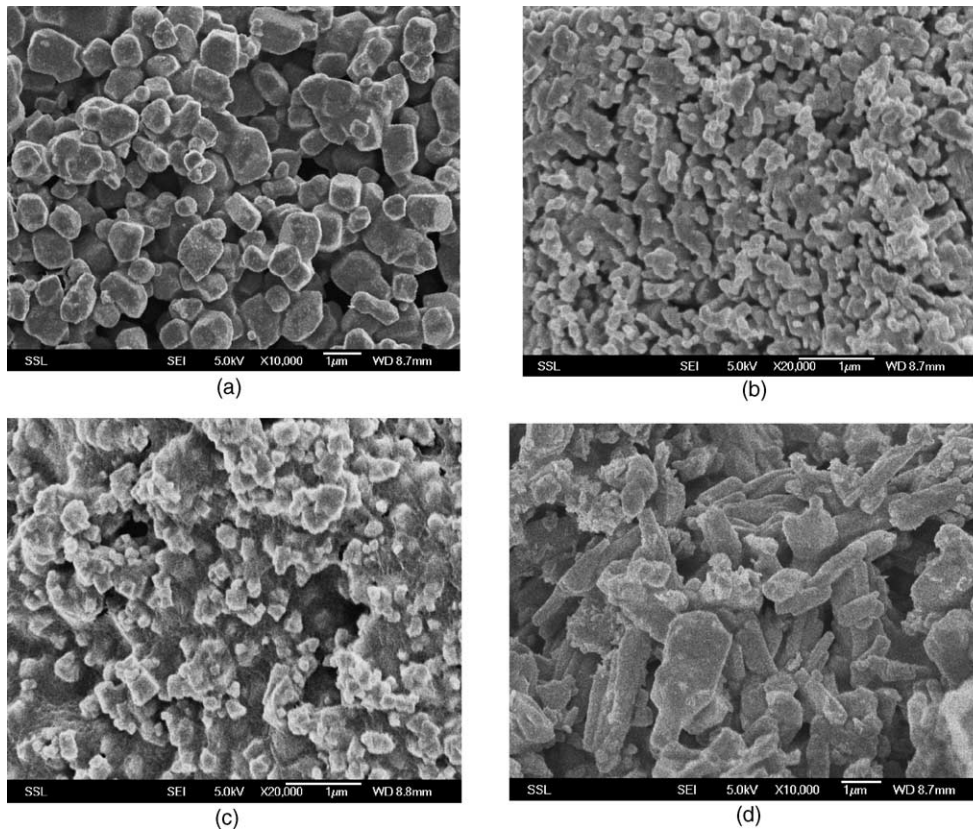
Fig. 2. SEM photographs: (a) SrSnO$_3$ (solid-state), (b) SrSnO$_3$ (sol–gel), (c) BaSnO$_3$ (solid-state), (d) Ca$_2$SnO$_4$. The white bar represents scale of 1 μm.

Table 1
XPS binding energies (BE, $\pm$0.1 eV) of Sn, O, Ca, Sr and Ba in compounds ASnO$_3$ (A = Ca, Sr, Ba), Ca$_2$SnO$_4$, SnO, SnO$_2$ and other compounds with perovskite structure

Compound	Element (region)	BE (eV)	References
CaSnO$_3$	Sn (3d$_{5/2}$; 3d$_{3/2}$)	485.7; 494.1 (Δ = 8.4)	This study
SrSnO$_3$		485.9; 494.3 (Δ = 8.4)	This study
BaSnO$_3$		485.4; 493.8 (Δ = 8.4)	This study
Ca$_2$SnO$_4$		486.3; 494.7 (Δ = 8.4)	This study
BaSnO$_3$		486.9	Manorama et.al. [34]
SnO/SnO$_2$		487.1;495.5(Δ = 8.4)	Ayouchi et. al. [35]
SnO$_2$		486.8; 495.2 (Δ = 8.4)	Barreca et al. [36]
CaSnO$_3$	O (1s)	529.3, 531.4	This study
SrSnO$_3$		529.4, 531.4	This study
BaSnO$_3$		528.7, 530.4	This study
Ca$_2$SnO$_4$		531.2	This study
BaSnO$_3$		530.2, 531.7, 533.2	Manorama et al. [34]
Bulk SnO		530.4	Jimenez et al. [39]
Bulk SnO$_2$		530.5	Barreca et al. [36]
LaMO$_3$ (M = Cr, Mn, Fe, Co, Ni)		528.3–528.9, 530.5–531.5	Yokoi et al. [37]
(La$_{0.4}$Sr$_{0.6}$) (Co$_{0.8}$Fe$_{0.2}$)O$_{3-\delta}$		529.2, 532.2	Machkova et al. [38]
CaSnO$_3$	Ca (2p$_{3/2}$; 2p$_{1/2}$)	346.2; 349.7 (Δ = 3.5)	This study
Ca$_2$SnO$_4$		346.9; 350.4 (Δ = 3.5)	This study
SrSnO$_3$	Sr (3d$_{5/2}$;3d$_{1/2}$)	132.7; 134.4	This study
(La$_{0.4}$Sr$_{0.6}$) (Co$_{0.8}$Fe$_{0.2}$)O$_{3-\delta}$		132.8; 134.2	Machkova et al. [38]
BaSnO$_3$	Ba (3d$_{5/2}$;3d$_{3/2}$)	778.1, 779.8; 793.8	This study
BaSnO$_3$		781.5	Manorama et al. [34]

Δ is difference in BEs.
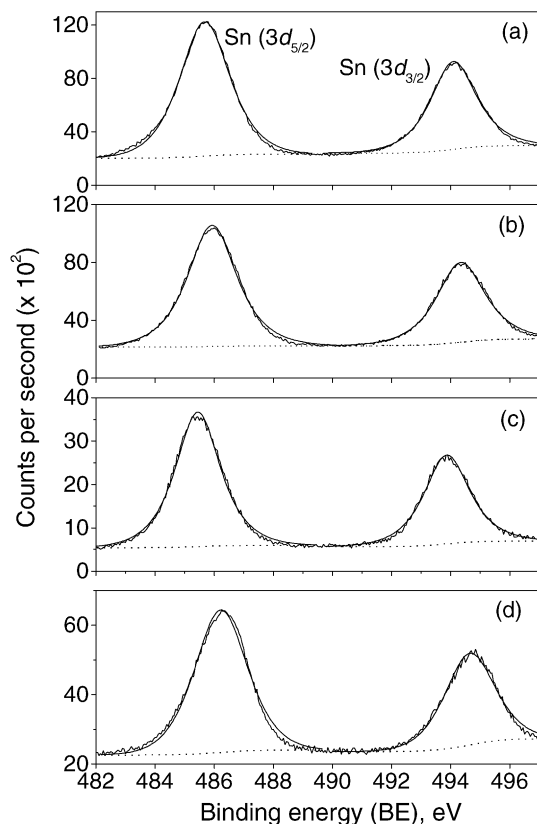
Fig. 3. XPS spectra in Sn-3d region of (a) CaSnO$_3$, (b) SrSnO$_3$, (c) BaSnO$_3$ and (d) Ca$_2$SnO$_4$. Base line and curve fitting of raw data are shown. 3d$_{5/2}$ and 3d$_{3/2}$ regions are indicated.

Fig. 4. XPS spectra in O ls region of (a) CaSnO$_3$, (b) SrSnO$_3$, (c) BaSnO$_3$, and (d) Ca$_2$SnO$_4$. Base line and curve fitting of raw data are shown.

gen octahedra and nine- or eight-fold oxygen co-ordination for the A-ions, have higher values than that of BaSnO$_3$. The O 1s spectrum for Ca$_2$SnO$_4$ (Fig. 4(d)) has only one peak at 531.2 eV and this is attributable to the lattice oxygen. It does not show any contribution from adsorbed oxygen. It is noted that the ASnO$_3$ compounds with the perovskite structures have been found to be conducive for the adsorption of gases and OH$^-$ species [34]. The O 1s peak for bulk SnO and SnO$_2$ occurs at 530.4 and 530.5 eV, respectively [36,39] (Table 1).

The best fit of XPS spectra of Ca 2p in CaSnO$_3$ and Ca$_2$SnO$_4$ shows that the resultant curve is a mixture of two overlapping peaks (Fig. 5(a) and (d)). These are attributed to Ca 2p$_{3/2}$ and 2p$_{1/2}$ with a BE separation of 3.5 eV. This result is in good agreement with BE values reported in the literature [31] with Ca 2p$_{3/2}$ at 346.6 eV and a 2p$_{3/2}$ and 2p$_{1/2}$ peak separation of 3.55 eV for CaS, CaCl$_2$, CaO, CaCO$_3$ and Ca(NO$_3$)$_2$. The spectrum of Sr 3d in SrSnO$_3$ (Fig. 5(b)) also comprises two peaks at 132.7 and 134.4 eV with a peak separation of 1.7 eV between the 3d$_{5/2}$ and 3d$_{3/2}$. This assignment is in agreement with the reported Sr 3d BE values, 132.8 and 134.2 eV in the oxide with the perovskite structure, (La$_{0.4}$Sr$_{0.6}$)(Co$_{0.8}$Fe$_{0.2}$)O$_{3-\delta}$ [38] (Table 1). The XPS of Ba 3d in BaSnO$_3$ (Fig. 5(c)) reveals an asymmetric peak that can be fitted into two peaks with BEs of, 778.1 (main)
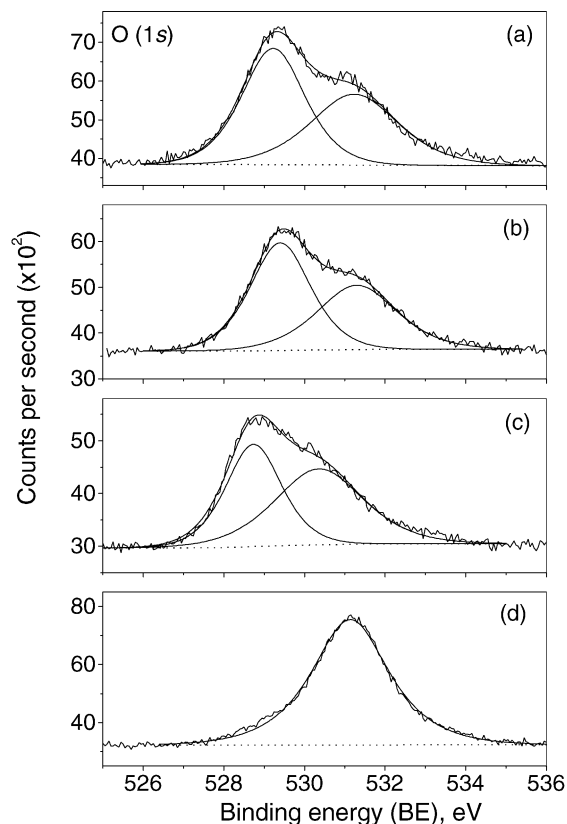
and 779.8 eV (small intensity). The second peak is symmetrical with a BE of 793.8 eV. The peaks at 778.1 and 793.8 eV are attributed to the Ba 3d$_{5/2}$ and 3d$_{3/2}$ in BaSnO$_3$ with a peak separation of 15.7 eV. This is different from the result of Manorama et al. [34], who reported only one peak in BaSnO$_3$ with a BE of 781.5 eV. According to Moulder et al. [31], the Ba 3d$_{5/2}$ peak in Ba-compounds (BaS, BaSO$_4$, BaCO$_3$, Ba(NO$_3$)$_2$ etc.) occurs at a BE of 780.6 eV with 3d$_{5/2}$−3d$_{3/2}$ = 15.33 eV. The latter value is comparable with that observed for BaSnO$_3$. The minor peak at 779.8 eV may be due to Ba 3d in BaO that is present as an impurity in BaSnO$_3$.

In summary, the XPS data clearly show that Sn^{4+} is present in ASnO$_3$ in an octahedral oxygen co-ordination (A = Ca, Sr, Ba) and Ca$_2$SnO$_4$. The A-ions are bivalent. The ASnO$_3$ has adsorbed oxygen on the surface of the particles.

3.2. Galvanostatic cycling

Voltage profiles and capacity versus cycle number plots are shown in Figs. 6–8 for ASnO$_3$ (A = Sr, Ba) and Ca$_2$SnO$_4$ at the constant current of 10 mA g^{-1} for the first two cycles and 30 and 60 mA g^{-1} during the subsequent cycles in the voltage range, 0.005–1.0 V. For the sake of comparison, the voltage profile for the first-discharge–charge cycle and the capacity versus cycle number plot for CaSnO$_3$ (sol–gel) from our previous studies [19,20] are shown in Fig. 8(b) and (c),
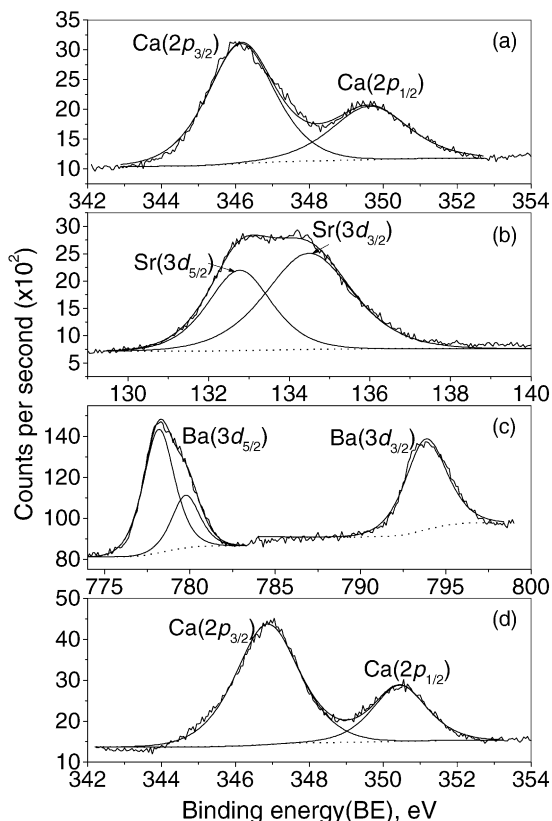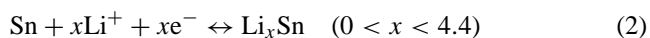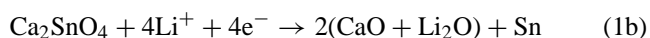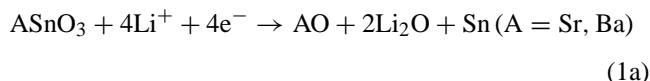
Fig. 5. XPS spectra in (a) Ca-2p region of CaSnO₃, (b) Sr 3d region of SrSnO₃, (c) Ba 3d region of BaSnO₃ and (d) Ca 2p region of Ca₂SnO₄. Base line and curve fitting of raw data are shown.

Fig. 6. The voltage vs. capacity profiles in voltage window, 0.005–1.0 V vs. Li for (a) SrSnO₃ (solid-state), (b) SrSnO₃ (sol–gel). Only select cycles are shown. Numbers represent cycles. (c) Capacity vs. cycle number plots for SrSnO₃ (solid-state and sol–gel). First two cycles at current density of $10\,\mathrm{mA\,g^{-1}}$, 3–22 cycles at $30\,\mathrm{mA\,g^{-1}}$ and 23–42 cycles at $60\,\mathrm{mA\,g^{-1}}$. First-discharge commences from open-circuit voltage (OCV). Open symbols: charge; filled symbols: discharge capacity.

respectively. The first-discharge profile for all the compounds differs from the rest of the charge and discharge profiles. It comprises a shoulder around 0.8–0.95 V, followed by a broad and relatively flat region in the voltage range, 0.7–0.1 V (versus Li) for ASnO₃ and Ca₂SnO₄.

The reaction mechanism for the initial discharge process can be assumed to be similar to that observed in CaSnO₃ and other Sn-metal oxides [2–4,6–9,11,12, 15–17,19,20], it being the crystal-structure destruction process that leads to the formation of active Sn-metal particles embedded in a AO (A = Ca, Sr, Ba) and lithia (Li₂O) matrix (Eq. 1(a) and (b)). The pristine nano-particles of Sn thus formed, undergo alloy formation with Li (Eq. (2)):

$$ASnO_3 + 4Li^+ + 4e^- \rightarrow AO + 2Li_2O + Sn\,(A = Sr, Ba)$$

$$\text{(1a)}$$

$$Ca_2SnO_4 + 4Li^+ + 4e^- \rightarrow 2(CaO + Li_2O) + Sn \quad \text{(1b)}$$

$$Sn + xLi^+ + xe^- \leftrightarrow Li_xSn \quad (0 < x < 4.4) \quad \text{(2)}$$

The AO compounds thus formed cannot be reduced to the A-metal state due to the high A−O bond strength [19,20,40–42] and these are electrochemically inactive with Li. We verified this experimentally by recording the galvanostatic response of super P carbon (C) and CaZrO₃ separately as cathodes versus Li. The electrode composition for the former is C:
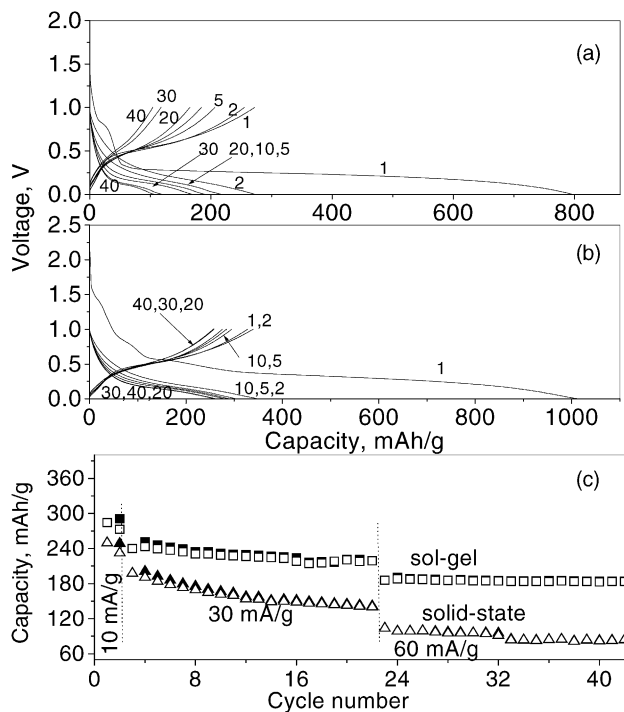
binder = 1:2 wt.% and that for the latter is CaZrO₃:C:binder = 65:20:15 wt.%. The voltage profile for super P carbon showed a plateau around ∼0.9 V during the first-discharge cycle, with a discharge capacity of $457\,\mathrm{mAh\,g^{-1}}$. The reversible charge–discharge capacity stabilized to $180\,\mathrm{mAh\,g^{-1}}$ at a current rate of $30\,\mathrm{mA\,g^{-1}}$ after a few cycles. The nature of the voltage profiles for CaZrO₃ is found to be exactly the same as those of super P carbon. From the electrode composition, an estimate of the capacity contribution from CaZrO₃ has been made after subtracting the value due to carbon. A negligible contribution (<10–$20\,\mathrm{mAh\,g^{-1}}$) is found for CaZrO₃, which thus reinforces the electrochemically-inert nature of CaO and ZrO₂ in CaZrO₃.

Although the electrochemically-active component (Sn) is same in all the compounds under investigation, there are significant variations in the over-all number of moles of Li-ions that react during the first-discharge cycle and the plateau voltage corresponding to the reduction of the oxide. Moreover, this plateau potential is different from that of pure SnO₂ (∼0.9 V), ATCO (1.2–1.7 V) and other Sn-oxides [1,2,6–8,12,15–17,19–20,43,44] in comparison with those of ASnO₃ and Ca₂SnO₄. This may be attributed to the effect of the crystal structure of the starting oxide, oxygen co-ordination, the counter (spectator) ion, and the compound morphology. Irvine and co-workers [2,8] have made similar observations in their studies on A₂SnO₄ (A = Mn, Co, Mg)
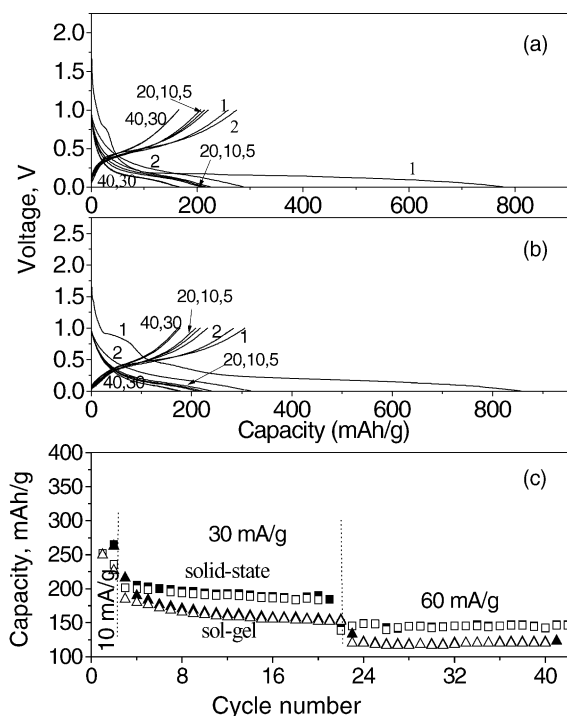
Fig. 7. Voltage vs. capacity profiles in voltage window, 0.005–1.0 V for (a) BaSnO$_3$ (solid-state), (b) BaSnO$_3$ (sol–gel). Only select cycles are shown. Numbers represent cycles. (c) Capacity vs. cycle number plots for BaSnO$_3$ (solid-state and sol–gel). First two cycles were performed at a current density of 10 mA g^{-1}, 3–22 cycles at 30 mA g^{-1} and 23–42 cycles at 60 mA g^{-1}. First-discharge commences from OCV. Open symbols: charge; filled symbols: discharge capacity.

Fig. 8. Voltage vs. capacity profiles in the voltage window, 0.005–1.0 V for (a) Ca$_2$SnO$_4$ (1–42 cycles). (b) CaSnO$_3$ (sol–gel) (first cycle; taken from [19]). Only selected cycles are shown. Numbers represent cycles. (c) Capacity vs. cycle number plots for Ca$_2$SnO$_4$ and CaSnO$_3$ (sol–gel). For Ca$_2$SnO$_4$, the first two cycles were performed at a current density of 10 mA g^{-1}, 3–22 cycles at 30 mA g^{-1} and 23–42 cycles at 60 mA g^{-1}. For CaSnO$_3$, first two cycles were done at a current density of 10 mA g^{-1}, 3–100 cycles at 60 mA g^{-1}. First-discharge commences from OCV. Open symbols: charge; filled symbols: discharge capacity.

with the inverse spinel structure, and have proposed that the variations in the plateau potential are the consequence of the differences in the matrix ion A. A plateau potential as low as 0.15 versus Li, which almost merges with the alloy formation (Li$_{4.4}$Sn) potential, was reported for Mg$_2$SnO$_4$. MgO was not reduced to Mg metal due to the large Mg–O bond strength. The sensitivity of the first-discharge profile towards the compound morphology was evident from the slight difference in the voltage profiles and the significant difference in the overall discharge capacity observed for SrSnO$_3$ and BaSnO$_3$ synthesized by solid-state and sol–gel techniques (Fig. 6(a and b) and Fig. 7(a and b)). Also, Ca$_2$SnO$_4$ shows the plateau potential at ~0.15 V unlike CaSnO$_3$ which shows at ~0.25 V (Fig. 8(a and b)). This can be attributed to the difference in the crystal structures of CaSnO$_3$ and Ca$_2$SnO$_4$ and the ratio of active host to inactive matrix element (Ca) content. As already mentioned, both compounds possess SnO$_6$ octahedra, but the Ca-ions are in nine-fold oxygen co-ordination in CaSnO$_3$ whereas in Ca$_2$SnO$_4$, they are in seven-fold co-ordination.

The first-charge sweep is the de-alloying process (reverse of Eq. (2)) and subsequent discharge–charge cycling takes place via the reversible Eq. (2) in the voltage range 0.005–1.0 V. These results are in agreement with those for the alloy formation reaction in other Sn-based compounds [2–4,6–8,15–17,43] and CaSnO$_3$ [19,20]. Electrode polarization effects have been observed for SrSnO$_3$ (solid-state)
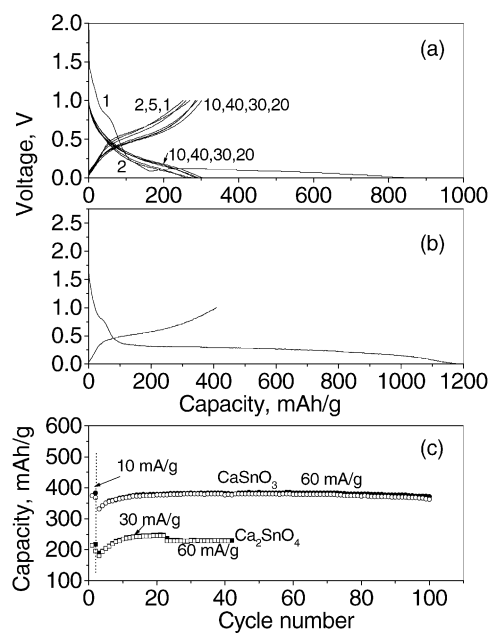
and BaSnO$_3$ (sol–gel and solid-state). The closely spaced charge–discharge profiles observed for Ca$_2$SnO$_4$ and SrSnO$_3$ (sol–gel) (Fig. 8(a) and Fig. 6(b)) show only small polarization and better cycling performance. Thus, from the voltage profiles, it is concluded that cycling cells with different electrode compositions and morphologies results in varying performances and reveals that the reversible capacity is a function of the composition, crystal structure and morphology of the electrode.

The electrochemical studies performed on super-P carbon, giving finite first-discharge and reversible discharge–charge capacity, show that the galvanostatic cycling results for the compounds under investigation are a summation of the capacity values from the compound and carbon (electronically conducting additive with 10/20 wt.% of the compound weight). The carbon participation is further supported by the occurrence of a shoulder around 0.9 V in the first-discharge profiles for the ASnO$_3$ and Ca$_2$SnO$_4$ compounds, i.e., at the same position as in the voltage profile of super-P carbon alone. Therefore, the C-contribution has been subtracted from the observed total capacities for all the cycles shown in Fig. 6(a and b), Fig. 7(a and b) and Fig. 8(a) These corrected values are shown as capacity versus cycle number plots in Fig. 6(c), Fig. 7(c) and Fig. 8(c) and select data are listed in Table 2. The corresponding moles of Li during the 1st, 20th and 40th cycles along with the theoretically expected values (from Eqs.

Table 2
Observed and theoretical discharge and charge capacities (mAh g⁻¹) (eq. moles of Li) for Sn-compounds

Compound; molecular weight (g)	Theoretical capacity first-discharge/first charge (moles of Li)	Observed first-discharg–charge capacity (moles of Li) at current rate (10 mA g⁻¹)	20th Discharge–charge capacity (moles of Li) at 30 mA g⁻¹	40th Discharge–charge capacity (moles of Li) at 60 mA g⁻¹
CaSnO₃ (sol–gel); 206.8 (From [19,20])	1088(8.4)/570(4.4)	1023(7.9)/375(2.9)	379(2.9)/377(2.9); at 60 mA g⁻¹	40th cycle: 382 (2.9)/377 (2.9) / 100th cycle: 372(2.9)/363(2.8)
SrSnO₃ (solid-state); 254.3	885(8.4)/464(4.4)	738(7.0)/250(2.4)	144(1.4)/143(1.4)	82(0.8)/82(0.8)
SrSnO₃ (sol–gel)		870(8.3)/284(2.7)	222(2.1)/221(2.1)	184(1.8)/183(1.8)
BaSnO₃ (solid-state); 303.9	741(8.4)/388(4.4)	721(8.2)/252(2.9)	190(2.2)/184(2.1)	142(1.6)/143(1.6)
BaSnO₃ (sol–gel)		715(8.1)/250(2.8)	156(1.8)/153(1.7)	122(1.4)/120(1.4)
Ca₂SnO₄ (sol–gel); 262.9	856(8.4)/449(4.4)	699(6.9)/214(2.1)	247(2.4)/246(2.4)	230(2.3)/229(2.3)

Voltage range: 0.005–1.0 V vs. Li.

(1) and (2)) are also given in Table 2. The observed capacities corresponding to the first-discharge reaction (Eq. (1)) given in Table 2 are lower than the theoretically expected ones for $SrSnO_3$ (solid-state) and Ca_2SnO_4, which possibly indicates incomplete reaction. The $SrSnO_3$ (sol–gel) and $BaSnO_3$ compounds exhibit values close to the expected ones. The subsequent first-charge capacities (reverse of Eq. (2)) in terms of moles of Li are small, namely: 2.7 Li for $SrSnO_3$ (sol–gel), 2.4 (solid-state); 2.9 for $BaSnO_3$ (solid-state); 2.8 (sol–gel); only 2.1 for Ca_2SnO_4 in comparison, the expected theoretical value is 4.4. Nevertheless these values compare well with that of $CaSnO_3$ (2.9 versus 4.4 Li, Table 2). Thus, there is a large irreversible capacity loss (ICL) in all these Sn-based compounds. It may be mentioned here that similar low values for the first-charge capacities have also been reported for other Sn-compounds e.g., Mg_2SnO_4: 2 mol of Li; Co_2SnO_4 [8] and $LiSn_2P_3O_{12}$: 3 mol of Li [2].

As can be expected, increasing the current density from 10 to 30 and/or 60 mA g⁻¹ after the 2nd and the 22nd cycle, respectively, decreases the reversible capacity of all the compounds. In all the cases, however the charge and discharge capacities are almost the same, which indicates that the coulombic efficiency is >98% (Fig. 6(c), Fig. 7(c), Fig. 8(c) and Table 2). $SrSnO_3$ (sol–gel) performs better than $SrSnO_3$ (solid-state) both in terms of capacity values and capacity degradation on cycling. A capacity of 246 mAh g⁻¹ on the 5th cycle degrades to 222 mAh g⁻¹ at the end of 20 cycles at a 30 mA g⁻¹ rate whereas in the range 21–40 cycles, the capacity of 190 mAh g⁻¹ degrades only to 183 mAh g⁻¹ at 60 mA g⁻¹ rate. The latter value corresponds to 1.8 Li moles which are recyclable (Fig. 6(c) and Table 2). On the other hand, for $SrSnO_3$ (solid-state) the capacity values at the end of 40 cycles correspond to recyclable Li of only 0.8 moles. The sol–gel synthesis yielding nano-particle morphology causes higher surface area (more reactive Sn-sites) and smaller diffusion lengths, which lead to high capacities. This is in agreement with our results on $CaSnO_3$ (sol–gel)[19,20] that gave better cycling performance (Table 2 and Fig. 8(c)).

In the case of $BaSnO_3$, the data (Table 2) show that solid-state synthesis gives slightly higher capacities than that of the sol–gel method at all current densities up to 42 cycles. This could be due to the high synthesis temperature (1200 °C) that is required to obtain single-phase material by both methods which causes agglomeration of particles and a sintering effect. We also noted that due to high molecular weight of the matrix (BaO), the theoretical recycleable-capacity of $BaSnO_3$ is only 388 mAh g⁻¹. The measured capacities are only in the range 120–140 mAh g⁻¹ at 60 mA g⁻¹ but these are stable between 22 and 42 cycles and correspond to recycleable Li = (1.5 ± 0.1) mol (Table 2 and Fig. 7(c)).

The capacity versus cycle number plot for Ca_2SnO_4 is shown in Fig. 8(c). Qualitatively, the response is same as that for $CaSnO_3$ (sol–gel) except that the capacity values are lower, namely, 247 mAh g⁻¹ at the end of 20 cycles at 30 mA g⁻¹ corresponding to 2.4 Li moles. In the case of $CaSnO_3$, the reversible capacity is ~380 mAh g⁻¹ (2.9 moles

of cycleable Li) and shows almost 100% capacity retention up to 100 cycles. In our earlier studies on $CaSnO_3$ [19,20], cycling was continued to 50 cycles. We have now extended the cycling up to 100 cycles at $60\,mA\,g^{-1}$ in the voltage range, 0.005–1.0 V; the data are shown in Fig. 8(c). Analogous to $CaSnO_3$, Ca_2SnO_4 shows good rate capability, i.e., upon doubling the discharge/charge current rate, the capacity decreases only by $17\,mAh\,g^{-1}$ ($\sim$7.0%). The higher Ca content in Ca_2SnO_4 as compared with $CaSnO_3$ does not provide any additional benefit and, on the contrary, has resulted in lower capacity values due to the larger inactive matrix content (CaO) per mole of the compound. One distinct feature observed in the cycling performances of Ca–Sn-compounds, when compared with those of Ba and Sr, is that the reversible capacity increases up to a few initial cycles and then an almost stable response is observed. This is due to the electrochemically insulating nature of the compound that is preventing the completion of the structure destruction process taking place during the first-discharge reaction and is spreading up to a few initial cycles (15 cycles in case of Ca_2SnO_4). In the case of $SrSnO_3$ and $BaSnO_3$, the capacity fading has started as early as the third cycle and thus this feature is not apparent.

A comparison of the electrochemical performance of $CaSnO_3$, $SrSnO_3$ and $BaSnO_3$ shows that the achievable capacity, the number of recycleable moles of Li, the rate capability and cycling stability decreases from Ca to Ba. This is possibly due to the increase in the atomic weight and ionic size in that order, which thereby enhances the inactive matrix metal content per mole of the composite electrode and the poorer inter-particle electronic conductivities that hinder the electron transfer.

For $SrSnO_3$, $BaSnO_3$ and Ca_2SnO_4, the best results are obtained with Ca_2SnO_4 in terms of the highest achievable capacities, the over-all number of cycleable Li-atoms, the low current-rate dependence and the good cycleability. This demonstrates that 'Ca' is a superior matrix element to Sr or Ba. The coulombic efficiency for all the compounds up to 40 cycles is >98%. We have shown the superior matrix behaviour of CaO in our studies on $CaSnO_3$ [19,20], $CaFe_2O_4$ and its solid solution with Sn [40], $Ca_2Fe_2O_5$ and $Ca_2Co_2O_5$ [41] and $CaMoO_4$ [42].

3.3. Cyclic voltammetry

Cyclic voltammetry is commonly used as a complimentary technique to establish the reversibility of electrode materials versus Li [2,19,22,32,33,43,44]. The CV curves for the compounds $SrSnO_3$ (sol–gel), $BaSnO_3$ (solid-state) and Ca_2SnO_4 in the voltage window 0.005–2.0 V up to 15 cycles at a scan rate of $0.058\,mV\,s^{-1}$, were recorded starting from a negative going scan (reduction of Sn^{4+} and alloy formation). Li metal acts as the counter and the reference electrodes. Selected cycles are shown in Fig. 9(a–c). The CV curves for $SrSnO_3$ at all cycles are similar except for intensity variations and slight shifts in the peak positions. The nature of these CV plots is somewhat similar to that
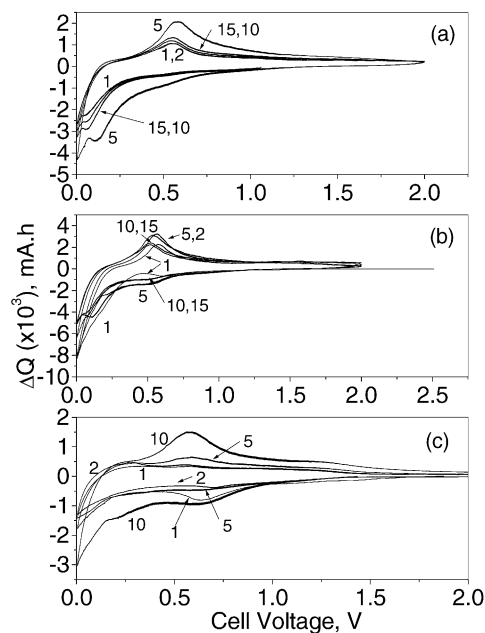

Fig. 9. Cyclic voltammograms (1–15 cycles) of (a) $SrSnO_3$ (sol–gel), (b) $BaSnO_3$ (solid-state) and (c) Ca_2SnO_4 vs. Li at a scan rate of $0.058\,mV\,s^{-1}$ and in voltage window 0.005–2.0 V. Only selected cycles are shown. Numbers represent cycles.

of $CaSnO_3$ [19,20], but differs from those of SnO_2 [22,44]. In pure SnO_2, the first-discharge reaction, i.e., the structure destruction process, is characterized by the existence of a peak around 0.9 V, which is not observed in $ASnO_3$ (A = Ca, Sr, Ba) and Ca_2SnO_4. In $SrSnO_3$, a small peak is observed at $\sim$0.05 V, which probably corresponds to the potential for Li–Sn alloy formation in the first-discharge. This is followed by an increase in $|\Delta Q|$ values up to the lower cut-off voltage. No peak is seen in the region below 0.5 V, which corresponds to the plateau potential in the galvanostatic discharge curve (Fig. 6(a)). The following charge reaction (anodic) comprises a peak at $\sim$0.55 V, which is due the de-alloying reaction and corresponds well with the plateau in Fig. 6(a) (reverse of Eq. (2)). The loop areas under the discharge and charge curves increase up to the fifth cycle. This shows the incomplete crystal structure destruction process continues up to five cycles. Thereafter, the decrease in the peak intensities signifies capacity fading, unlike the results in the galvanostatic cycling mode, where almost stable behaviour is observed at a given current rate in the voltage range 0.005–1.0 V versus Li. The CV to the higher cut-off voltage of 2.0 V causes the irreversible destruction of lithia and leads to the agglomeration of Sn particles and possible Sn-oxide formation. The larger particles are the cause of severe volume changes and life capacity fading. This effect of the operating voltage range on cycling performance has been demonstrated by us for $CaSnO_3$ [20] and by others in the case of Sn-compounds [2,16,17,24], and a good operating voltage range was found to be 0.005–1.0 V. By contrast, no distinct features are observed in the anodic CV profiles for $SrSnO_3$ that indicate lithia destruction up to 2.0 V (Fig. 9(a)), whereas

a peak at ∼1.35 V due to the latter was clearly observed for $CaSnO_3$ [20].

The CV of $BaSnO_3$ (Fig. 9(b)) resembles that of $SrSnO_3$, except that the irreversible structure destruction process (first-discharge) continues up to the lower cut-off voltage. Cathodic and anodic peaks that occur at 0.1 and 0.55 V versus Li, respectively, characterize the alloying/de-alloying reactions in the subsequent cycles. The anodic loop area is enhanced in sweeps up to the fifth cycle and diminishes thereafter, which indicates capacity fading. The anodic peak at 0.55 V matches well with the plateau region in the voltage profile shown in Fig. 7(b).

The behaviour of the CV for Ca_2SnO_4 (Fig. 9(c)) during the first few cycles is similar to those for $ASnO_3$, (A = Sr, Ba) in that no clear peaks are observed and the over-all intensity is distributed over the entire loop. On the other hand, the first-discharge curve does show a peak at ∼0.7 V and this corresponds to the small voltage plateau in the galvanostatic discharge curve (Fig. 8(a)). The anodic peak at ∼0.55 V develops clearly during 5–10 cycles and corresponds to the plateau voltage in Fig. 8(a). Broad cathodic and anodic peaks that are centered at ∼0.65 and 1.25 V respectively, are also present. This indicates the involvement of Li_2O and Sn to form SnO/SnO_2 which is detrimental to the performance of Sn-based compounds as good anodes in lithium-ion batteries. This has been shown in CV and galvanostatic cycling of $CaSnO_3$ [20]. Hence charge–discharge cycling should be restricted to the voltage window 0.005–1.0 V for $ASnO_3$ and Ca_2SnO_4 to obtain stable and reversible capacities with good coulombic efficiency.

4. Conclusions

Exploratory studies have been carried out on the compounds $ASnO_3$ (A = Sr, Ba) with the perovskite structure and Ca_2SnO_4 with the Sr_2PbO_4-type structure to examine their suitability as anodes for lithium-ion batteries. The results are compared with those for $CaSnO_3$ reported by us earlier. The compounds are synthesized by solid-state and/or sol–gel methods, characterized by XRD, XPS, SEM, and their electrochemical behaviour is evaluated by galvanostatic cycling and cyclic voltammetry as cathodes versus Li. $SrSnO_3$ (sol–gel) shows a nano-particle morphology in contrast to the μm-size particles obtained by the solid-state method. The electrochemical cycling takes place via a reversible Li–Sn alloying–de-alloying reaction in the voltage range 0.005–1.0 V. The discharge capacities (mAh g^{-1}) (moles of Li) at the 20th cycle at a current rate of 30 mA g^{-1} are: $SrSnO_3$ (solid-state) (144 (1.4)), $SrSnO_3$ (sol–gel) (222 (2.1)), $BaSnO_3$ (solid-state) (190 (2.2)), $BaSnO_3$ (sol–gel) (156 (1.8)) and Ca_2SnO_4 (247 (2.4)). The coulombic efficiencies are >98% in all cases. These reversible capacities are only slightly lower when the current rate is increased to 60 mA g^{-1} and remain fairly stable in the range 20–42 cycles, except for $SrSnO_3$ (solid-state) which shows a small

degradation. This demonstrates the good rate-capability of the compounds. The performance of $SrSnO_3$ (sol–gel) is superior to that of $SrSnO_3$ (solid-state), which highlights the importance of nano-particle morphology. By contrasts performance of $ASnO_3$ (A = Sr, Ba) is inferior when compared with that of iso-structural $CaSnO_3$ which thereby shows that Ca is a more advantageous 'spectator' ion in the perovskite matrix. Although Ca_2SnO_4 performs better than $ASnO_3$ in giving 2.3 mol of recyclable Li (at 60 mA g^{-1}; 40th cycle), it is inferior to $CaSnO_3$ (2.9 mol of recyclable Li). This indicates that increasing the Ca:Sn atom ratio to 2:1 does not give any benefits and that the perovskite structure is preferable to that of the Sr_2PbO_4-type. CV studies support the results from galvanostatic cycling.

References

[1] Y. Idota, T. Kubota, A. Matsufuji, Y. Maekawa, T. Miyasaka, Science 276 (1997) 1395–1397.
[2] M. Behm, J.T.S. Irvine, Electrochim. Acta 47 (2002) 1727–1738.
[3] I.A. Courtney, J.R. Dahn, J. Electrochem. Soc. 144 (1997) 2045–2052.
[4] M. Winter, J.O. Besenhard, Electrochim. Acta 45 (1999) 31–50.
[5] F. Chen, Z. Shi, M. Liu, Chem. Commun. (2000) 2095–2096.
[6] K. Wan, S.F.Y. Li, Z. Gao, K.S. Siow, J. Power Sources 75 (1998) 9–12.
[7] Z. Yuan, F. Huang, J. Sun, Y. Zhou, Chem. Lett. (Jpn.) (2002) 408–409.
[8] P.A. Connor, J.T.S. Irvine, J. Power Sources 97–98 (2001) 223–225.
[9] P.A. Connor, J.T.S. Irvine, Electrochim. Acta 47 (2002) 2885–2892.
[10] O. Mao, J.R. Dahn, J. Electrochem. Soc. 146 (1999) 423–427.
[11] J. Read, D. Foster, J. Wolfenstine, W. Behl, J. Power Sources 96 (2001) 277–281.
[12] J.Y. Lee, Y. Xiao, Z. Liu, Solid State Ionics 133 (2000) 25–35.
[13] M. Wachtler, J.O. Besenhard, M. Winter, J. Power Sources 94 (2001) 189–193.
[14] Z. Peng, Z. Shi, M. Liu, Chem. Commun. (2000) 2125–2126.
[15] M. Wachtler, M. Winter, J.O. Besenhard, J. Power Sources 105 (2002) 151–160.
[16] I.A. Courtney, W.R. McKinnon, J.R. Dahn, J. Electrochem. Soc. 146 (1999) 59–68.
[17] I.A. Courtney, J.R. Dahn, J. Electrochem. Soc 144 (1997) 2943–2948.
[18] L. Fang, B.V.R. Chowdari, J. Power Sources 97–98 (2001) 181–184.
[19] N. Sharma, K.M. Shaju, G.V. Subba Rao, B.V.R. Chowdari, Electrochem. Commun. 4 (2002) 947–952.
[20] N. Sharma, K.M. Shaju, G.V. Subba Rao, B.V.R. Chowdari, in: B.V.R. Chowdari, S.R.S. Prabaharan, M. Yahaya (Eds.), Solid State Ionics: Trends in the New Millennium, World Scientific, Singapore, 2002, pp. 87–95.
[21] N. Li, C.R. Martin, J Electrochem. Soc. 148 (2001) A164–A170.
[22] T. Brousse, R. Retoux, U. Herterich, D.M. Schleich, J. Electrochem. Soc. 145 (1998) 1–4.
[23] S.C. Nam, Y.H. Kim, W.I. Cho, B.W. Cho, H.S. Chun, K.S. Yun, Electrochem. Solid-State Lett. 2 (1999) 9–11.
[24] M. Mohamedi, S.-J. Lee, D. Takahashi, M. Nishizawa, T. Itoh, I. Uchida, Electrochim. Acta 46 (2001) 1161–1168.
[25] A.-M. Azad, L.L.W. Shyan, P.T. Yen, J. Alloys Compd. 282 (1999) 109–124.
[26] C.P. Udawatte, M. Kakihana, M. Yoshimura, Solid State Ionics 108 (1998) 23–30.

[27] A. Vegas, M. Vallet-Regi, J.M. Gonzalez-Calbet, M.A. Alario-Franco, Acta Crystallogr. Sect. B 42 (1986) 167–172.

[28] L.A. Martinez-Cruz, A. Ramos-Gallardo, A. Vegas, J. Solid State Chem. 110 (1994) 397–398.

[29] Hk. Muller-Buschbaum, J. Alloys Compd. 349 (2003) 49–104.

[30] J.E. Fiscus, H.C. zur Loye, J. Alloys Compd. 306 (2000) 141–145.

[31] J.F. Moulder, W.F. Stickle, P.E. Sobol, I.L.P. Bomben, in: J. Chastain, R.C. King Jr. (Eds.), Handbook of X-Ray Photoelectron Spectroscopy, Physical Electronics Inc., Minnesota, 1995.

[32] K.M. Shaju, G.V. Subba Rao, B.V.R. Chowdari, Solid State Ionics 152–153 (2002) 69–81.

[33] K.M. Shaju, G.V. Subba Rao, B.V.R. Chowdari, Solid State Ionics 148 (2002) 343–350.

[34] S.V. Manorama, C.V. Gopal Reddy, V.J. Rao, Appl. Surf. Sci. 174 (2001) 93–105.

[35] R. Ayouchi, F. Martin, J.R.R. Barrado, M. Martos, J. Morales, L. Sanchez, J. Power Sources 87 (2000) 106–111.

[36] D. Barreca, S. Garon, E. Tondello, P. Zanella, Surf. Sci. Spectra 7 (2000) 81–85.

[37] Y. Yokoi, H. Uchida, Catal. Today 42 (1998) 167–174.

[38] M. Machkova, N. Brashkova, P. Ivanov, J.B. Carda, V. Kozhukharov, Appl. Surf. Sci. 119 (1997) 127–136.

[39] V.M. Jimenez, J.P. Espinos, A.R.G. Elipe, Surf. Sci. 366 (1996) 556–563.

[40] N. Sharma, K.M. Shaju, G.V. Subba Rao, B.V.R. Chowdari, J. Power Sources 124 (2003) 204–212.

[41] N. Sharma, K.M. Shaju, G.V. Subba Rao, B.V.R. Chowdari, Electrochim. Acta 49 (2004) 1035–1043.

[42] N. Sharma, K.M. Shaju, G.V. Subba Rao, B.V.R. Chowdari, Z.L. Dong, T.J. White, Chem. Mater. 16 (2004) 504–512.

[43] W. Liu, X. Huang, Z. Wang, H. Li, L. Chen, J. Electrochem. Soc. 145 (1998) 59–62.

[44] S. Machill, T. Shodai, Y. Sakurai, J. Yamaki, J. Power Sources 75 (1998) 216–223.